Research article

Derivation, parameterization and validation of a creep deformation/rupture material constitutive model for SiC/SiC ceramic-matrix composites (CMCs)

Mica Grujicic *, Rohan Galgalikar, S. Ramaswami, and Jennifer S. Snipes

Department of Mechanical Engineering, Clemson University, Clemson SC 29634, USA

* Correspondence: Email: gmica@clemson.edu; Tel: +1-864-656-5639; Fax: +1-864-656-4435.

Abstract: The present work deals with the development of material constitutive models for creep-deformation and creep-rupture of SiC/SiC ceramic-matrix composites (CMCs) under general three-dimensional stress states. The models derived are aimed for use in finite element analyses of the performance, durability and reliability of CMC turbine blades used in gas-turbine engines. Towards that end, one set of available experimental data pertaining to the effect of stress magnitude and temperature on the time-dependent creep deformation and rupture, available in the open literature, is used to derive and parameterize material constitutive models for creep-deformation and creep-rupture. The two models derived are validated by using additional experimental data, also available in the open literature. To enable the use of the newly-developed CMC creep-deformation and creep-rupture models within a structural finite-element framework, the models are implemented in a user-material subroutine which can be readily linked with a finite-element program/solver. In this way, the performance and reliability of CMC components used in high-temperature high-stress applications, such as those encountered in gas-turbine engines can be investigated computationally. Results of a preliminary finite-element analysis concerning the creep-deformation-induced contact between a gas-turbine engine blade and the shroud are presented and briefly discussed in the last portion of the paper. In this analysis, it is assumed that: (a) the blade is made of the SiC/SiC CMC; and (b) the creep-deformation behavior of the SiC/SiC CMC can be represented by the creep-deformation model developed in the present work.

Keywords: ceramic-matrix composites; material constitutive models; creep deformation; creep rupture

1. Introduction

The present work addresses the problem of creep-deformation and creep-rupture under multiaxial loading conditions in SiC-reinforcement/SiC-matrix ceramic-matrix composites (CMCs). The main objective of the present work is to develop the appropriate creep-deformation and creep-rupture material models which, when implemented in the appropriate user-defined material subroutines and coupled with commercial, open-source or proprietary finite-element solvers, can be used to analyze creep-/creep-rupture-controlled performance and durability of various gas-turbine engine-based CMC components. Consequently, the concepts most relevant to the present work are: (a) the basics of ceramic-matrix composites; (b) creep and creep-rupture of high-temperature structural materials; (c) prior experimental work concerning creep behavior of SiC/SiC CMCs; and (d) prior modeling work concerning creep behavior of SiC/SiC CMCs. In the remainder of this section, a brief description is provided for each of these concepts.

1.1. The basics of ceramic-matrix composites

The high-temperature metallic materials used in gas-turbine engines (such as nickel-, cobalt- or iron-based superalloys) are often made to operate at temperatures within 50 K of their melting points, and so have been pushed to their thermal-stability limit. To increase power density and energy efficiency of the gas-turbine engines, new materials are needed which can operate at temperatures as high as 1500 K. The main candidate materials currently identified for use in the next generation of gas-turbine engines are (monolithic) ceramics and CMCs. Since these materials can withstand extremely high temperatures, their use in hot sections of gas-turbine engines can yield a number of benefits such as: (i) improvements in thrust and fuel efficiency; (ii) lower pollutant emissions; (iii) reduced cooling requirements; (iv) simplification of the engine-component design; and (v) reduced requirements for the strength/weight of the supporting structure.

Unfortunately, monolithic ceramics are not being perceived as respectable candidate materials for use in critical turbine-engine structural applications (e.g. turbine shroud segments, vanes and blades), since they have relatively low fracture toughness, tensile strength and damage tolerance. On the other hand, CMCs consisting of a ceramic matrix and ceramic fibers possess superior structural properties (including non-catastrophic nature of failure) relative to their monolithic-ceramic counterparts, while retaining their high-temperature stability and integrity. This is the reason that the CMCs are being aggressively researched and developed for use in future gas-turbine engines. The potential of the CMCs in revolutionizing the performance of the gas-turbine engines is shown schematically in Figure 1 [1]. In this figure, the x-axis represents the approximate period of dominance in usage of the particular class of high-temperature materials (and associated cooling technologies), while the y-axis denotes the temperature capability of the material class in question. It is seen that the temperature capability of CMCs lies above the fitting line for the temperature capabilities of the past and present gas-turbine engine materials.

CMCs were initially perceived as candidate materials in gas-turbine engine components which experience low in-service loads, such as nozzles, combustion liners, shroud segments and exhaust components. Currently, these components have reached the commercialization stage, and are being employed in the engines of 200-seater aircraft [2]. In addition, CMCs have been successfully tested for use in low-pressure turbine blades in military aircraft engines [3]. In the case of

rotating/revolving components like blades, the sustained presence of the centrifugal forces combined with high temperatures can lead to CMC excessive creep-deformation and/or creep-rupture. Consequently, detailed understanding of the CMC-creep behavior is critical in designing such components and ensuring their required durability and reliability.
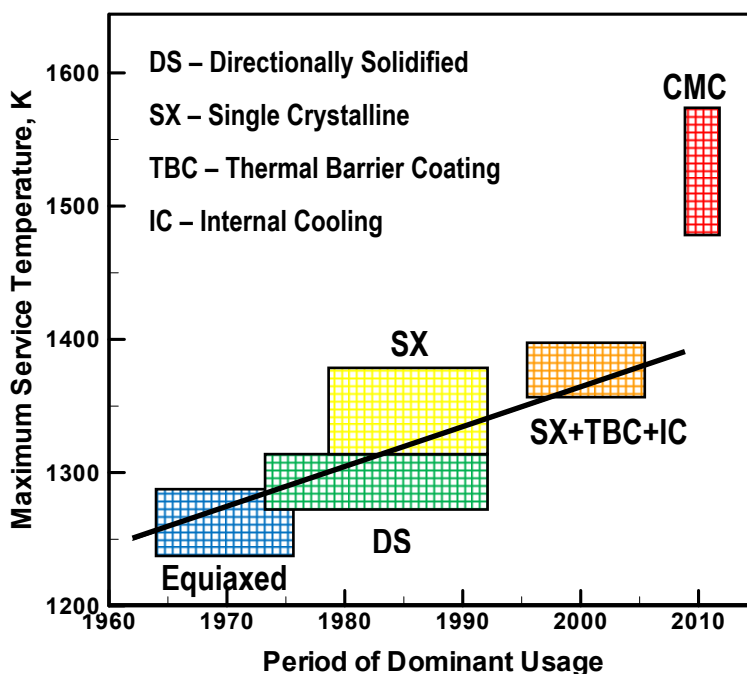

Figure 1. Temperature capability (i.e. maximum service temperature) and time period of dominant usage, of different materials used in gas-turbine engines.

1.2. Creep-deformation and creep-rupture of high-temperature structural materials

When a material is subjected to sustained loading at elevated temperature, it undergoes time-dependent inelastic deformation known as creep deformation. Typically, creep occurs at homologous temperatures greater than approximately 0.5 (the homologous temperature is defined as the ratio of the exposure temperature and material melting point, both expressed in kelvin) and at stress levels which are lower than those required to induce inelastic deformation under monotonic loading conditions [4]. Excessive creep deformation is typically followed by material fracture, commonly referred to as "creep rupture." Figure 2 shows typical variation of the creep strain with time. In Figure 2, two creep-strain vs. time curves are depicted. The lower one is associated with stress level σ_1 and temperature T_1, while the upper curve is associated with one of the following three conditions:

(i) $\sigma_2 > \sigma_1$, $T_2 = T_1$; (ii) $\sigma_2 = \sigma_1$, $T_2 > T_1$; and (iii) $\sigma_2 > \sigma_1$, $T_2 > T_1$. Examination of Figure 2 reveals that a creep-strain vs. time curve consists of three segments, each reflecting a different stage of creep deformation:

(a) in the primary creep regime, Section 1, the creep strain rate (numerically equal to the slope of the curve) decreases monotonically with time due to the operation of strain-hardening processes [5];

(b) in the steady-state or secondary creep regime, Section 2, the material creeps at a constant rate due to a balance of the strain-hardening and strain-softening mechanisms [6]; and

(c) in the final or tertiary creep regime, Section 3, the creep rate increases significantly due to the operation of material-degradation processes such as cavity formation, growth and coalescence. When the material has sustained a threshold level of damage, it ruptures [7].

It should be noted that the major portion of the rupture time (total creep time before rupture) is taken up by the steady-state regime of creep, so the *x*-axis in Figure 2 is not drawn to scale. In design applications in which excessive creep deformation is of primary concern, the steady-state or minimum creep rate at the operating stress and temperature conditions is used as the primary creep-resistance material parameter. In other applications in which creep-rupture is of key concern, rupture time is used as the primary creep-resistant material parameter. Examination of Figure 2 shows that as the stress and/or temperature are increased, the steady-state creep rate increases while the rupture time decreases. Thus, excessive creep deformation and creep-rupture problems are associated with higher stresses and/or higher temperatures.
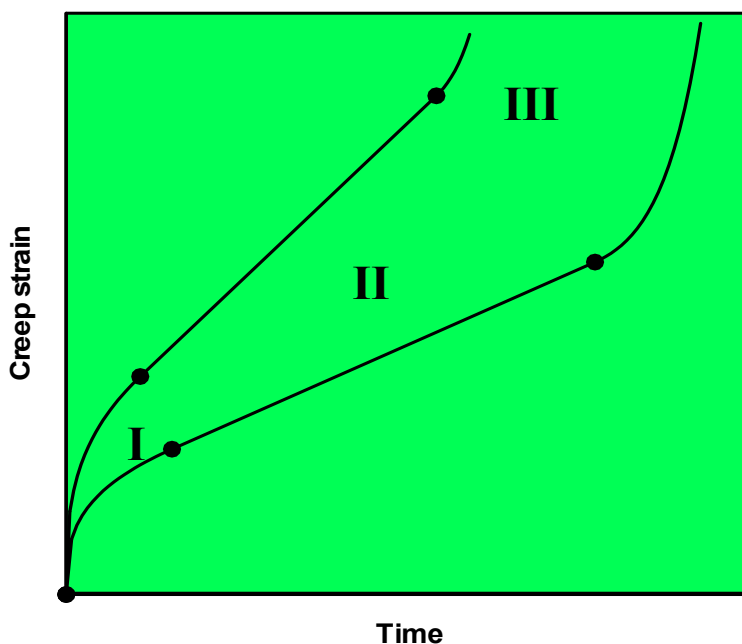

Figure 2. Typical evolution of creep strain. For the lower curve, the stress is fixed at σ_1 and the temperature at T_1. For the upper curve, one of three conditions holds: (a) $\sigma_2 > \sigma_1$, $T_2 = T_1$; (b) $\sigma_2 = \sigma_1$, $T_2 > T_1$; and (c) $\sigma_2 > \sigma_1$, $T_2 > T_1$. The three segments of each curve correspond to the: (i) initial; (ii) steady-creep; and (iii) terminal stages of creep deformation.

Demands for greater power, reduced weight, improved fuel economy, and lower life-cycle costs are the main factors influencing gas-turbine engine designs. Higher combustion temperatures are a

key to meeting these requirements. It is generally accepted that the maximum attainable performance of the gas-turbine engine is controlled by the maximum allowable temperature of the turbine rotor/blades, and that excessive creep-deformation and potential creep-rupture of the turbine blades control the maximum allowable temperature. As far as the stresses experienced by the blades are concerned, they primarily originate from three sources: (i) centrifugal forces due to high rotation speeds; (ii) bending stresses due to the momentum of the high-pressure high-velocity combustion gases; and (iii) thermal stresses due to non-uniformity in temperature and mismatches in thermal expansion coefficients with the adjoining components.

Creep deformation manifests itself as blade elongation under normal operating conditions. Blade elongation is monitored during operation using various sensors mounted on the engine casings, including eddy current, discharging probe, capacitive, inductive, microwave, and infrared sensors. As part of the regular inspection, blade elongation is measured and the tip of each blade trimmed to maintain the correct tip clearance. Retention of the correct tip clearance is critical since insufficient clearance may lead to the blade tip making contact with the non-rotating shroud, causing a "tip rub" which necessitates dismantling of the engine for repair and quite probably replacement of both blades and shroud. On the other hand, excessive clearance compromises gas-turbine engine efficiency since combustion gases escape from the main flow path. Following several blade-tip trimming operations, after the blades have experienced a predetermined total elongation, they are replaced in order to avoid creep-induced blade rupture (typically in the region where the blade is mounted to the high-speed rotating hub). In the case of gas-turbine engines used in aviation applications, blade inspection is carried out typically after every 2000 hours of operation, while the rotor overhaul is conducted typically after every 5000 hours. In the case of ground power or marine applications, the inspection and overhaul hours are substantially longer.

1.3. Prior experimental work concerning creep behavior of SiC/SiC CMCs

Many studies have been published on the creep behavior of oxide-based CMCs (not the subject of the present work), but apparently only four studies on the creep behavior of SiC/SiC CMCs (the subject of the present work). In the remainder of this subsection, the latter four studies are briefly overviewed.

Corman and Luthra [1] studied the creep behavior of prepreg melt-infiltrated SiC/SiC CMCs in uniaxial-stress loading experiments. The results obtained are summarized in Table 1 and in Figure 3. Table 1 contains six columns, with each column providing the following information: (i) sample identification; (ii) test temperature (°C); (iii) applied uniaxial stress (MPa); (iv) rupture time; (v) total strain at failure or at creep run-out time of 1000 hours; and (vi) creep rate at 1000 hours (1/s), if applicable. Examination of this table reveals that:

(a) at 816 °C and applied uniaxial stresses of 125 MPa and 140 MPa, creep deformation cannot be detected. The specimen 704A-2 tested at 816 °C and 140 MPa failed not due to creep but rather due to the presence of a potent pre-existing flaw;

(b) the measured creep rates at 1000 hours are quite small, and if these creep rates are multiplied by the run-out time of 1000 hours, the resulting creep strains are substantially lower than their counterparts, obtained by subtracting from the total strains reported in the fifth column of Table 1 the corresponding elastic strains. This finding suggests that within the time period of 1000 hours, the

subject CMC was in the primary regime of creep, the regime in which the creep rate continuously decreases as a function of time; and

(c) at the highest temperatures employed, 1093 °C and 1204 °C, the tests conducted did not conclusively identify a lower bound of stress below which creep rupture does not take place.

Figure 3 shows the effect of the magnitude of the applied uniaxial stress, at 1093 °C and 1204 °C, on the rupture time. As expected, it is seen that an increase in stress and/or temperature results in a lower rupture time.

Morscher and Pujar [8] studied the creep behavior of SiC/SiC CMCs at 1315 °C, for uniaxial stresses from 100 to 170 MPa, and a creep run-out time of 100 h. The results obtained revealed a superior creep resistance of the subject materials relative to the competing grades of the CMCs. In addition, post-creep fast-fracture testing of the CMCs revealed that creep deformation within the CMCs slightly increased the first matrix-cracking stress. This finding was attributed to the effect of the stress redistribution between the matrix and the fibers, which reduces the tensile-stress level within the matrix and, hence, delays the onset of matrix cracking.

Morscher et al. [9] also studied the creep, dwell fatigue and cyclic fatigue behavior of SiC/SiC CMCs at 1204 °C, in a 180–220 MPa stress range in air. (The CMCs consisted of Sylramic-iBN SiC fibers, BN fiber interphase coating, and slurry-cast melt-infiltrated (MI) SiC-based matrix.) Specimens which did not fail during fatigue testing were subsequently fast-fractured in order to assess the extent of creep-induced material degradation. The results obtained revealed losses of ca. 20% in strength and 10% in stiffness after creep for 100 hours at the highest stress levels applied and after 2000 hours at the lowest stresses applied. The previously mentioned creep-induced increase in the first matrix-cracking stress was again observed.
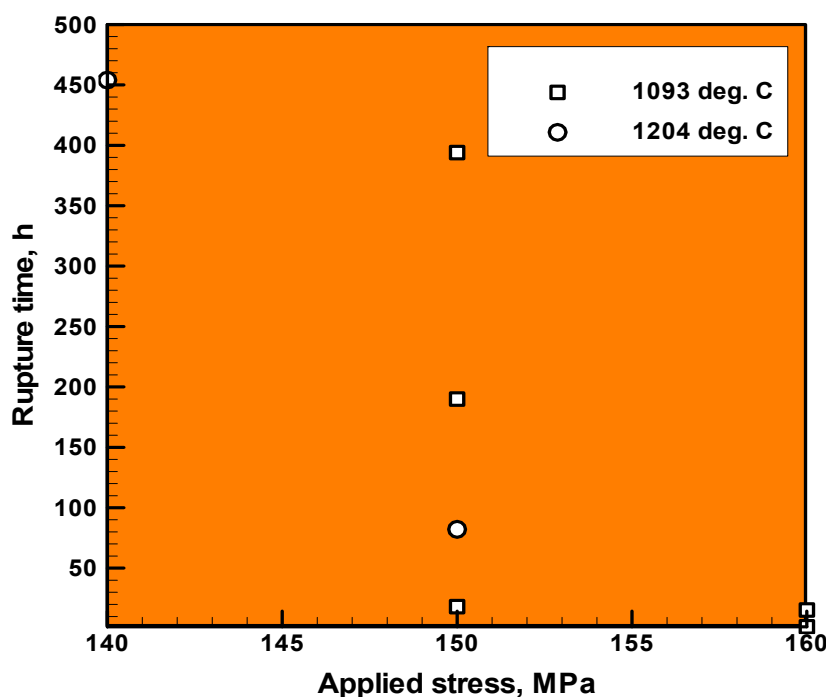

Figure 3. Variation of creep-rupture time with the magnitude of the applied uniaxial stress, for prepreg melt-infiltrated SiC/SiC CMCs [1].

van Roode et al. [10] investigated creep behavior of two grades of SiC/SiC CMCs, one based on Hi-Nicalon fibers (whose nanometer grain size and lack of stoichiometry lead to inferior creep resistance) and the other based on Sylramic-iBN fibers (whose substantially larger grain size and higher degrees of stoichiometry and crystallinity lead to superior creep resistance). The results obtained revealed that in the absence of strong oxidizing-environmental conditions the latter grade of CMCs possesses superior creep-rupture properties, while in the presence of such conditions, creep-rupture properties of the two CMC grades are quite comparable. In addition, it is found that if the CMCs are protected using environmental barrier coatings, the CMC grade based on Sylramic-iBN fibers again displays superior creep-rupture properties even in the presence of strong oxidizing environmental conditions.

1.4. Prior modeling work concerning creep behavior of SiC/SiC CMCs

Four published studies of modeling the creep behavior of SiC/SiC CMCs have been identified. These four studies are briefly reviewed in the remainder of this subsection, and the main contributions and shortcomings of these studies have been identified.

Rospars et al. [11] investigated creep behavior of plain-woven SiC/SiC CMCs through experiments and computations, and tried to model creep-induced material damage on the basis of continuum damage-mechanics. To quantify the extent and diversity of local damage, damage variables are introduced for each mode of material damage. Creep deformation is modeled as a time-dependent inelastic deformation process, and particular attention is devoted to identifying the appropriate creep-deformation potential, the gradient of which is used within the flow-rule functional relationship to model the progress of creep. The main emphasis in the work of Rospars et al. [11] was on deriving and parameterizing the creep-induced damage-parameter evolution equations. However, no attempt was made to either predict the creep rupture as a function of the imposed multiaxial stress and temperature conditions, or to derive a creep-deformation material constitutive model for the general case of multiaxial loading.

Rugg et al. [12] studied the creep behavior of SiC/SiC CMC microcomposites consisting of a single SiC fiber coated with carbon and surrounded by SiC matrix, with or without matrix cracking. Creep behavior of the microcomposite was directly compared with that of the fiber and the matrix. In order to relate the creep behavior of the microcomposite to that of the fiber and the matrix, simple phenomenological models have been developed. While the work of Rugg et al. [12] provides a new insight into the creep behavior of the CMCs, which is not generally gained in the case of bulk CMCs, the models developed could not be readily applied to bulk CMCs, even under uniaxial-loading conditions.

Chermant et al. [13] investigated the creep mechanism(s) in CMCs with both crystalline-ceramic and glassy-ceramic matrices, using experiments and theory. The results obtained suggest that in chemical vapor infiltrated (CVIed) CMCs with a crystalline-ceramic matrix like SiC/SiC CMCs, the creep deformation and rupture involve the operation of the following time-dependent processes: (a) matrix cracking; (b) matrix/fiber interfacial shear and debonding; and (c) conventional creep of the fibers bridging the matrix cracks. The experimental results clearly established that the tertiary regime of creep is absent in SiC/SiC CMCs, i.e. creep rupture occurs in the secondary regime of creep. To model the creep-deformation and ultimate creep-rupture processes, a damage-mechanics framework was utilized, within which damage variables involved during creep, are utilized to

Table 1. Summary of the tensile creep rupture testing results on GE prepreg MI composites made in July September, 2000 with GEGR optimized Configuration C fiber coating on Hi-Nicalon fiber. All testing was performed in air [1].

Specimen	Temp. (°C)	Creep Stress (MPa)	Rupture time § (h)	Failure strain * (%)	Creep rate at 1000 hours
730-1	816	125	>1000	0.07	$<10^{-11}$
704A-2[a]	816	140	460.2	0.05	–
732-2	816	140	>1000	0.08	$<10^{-11}$
717-2	816	140	>1000	0.08	$<10^{-11}$
704A-1[a]	1093	125	>1000	0.03	2.6×10^{-11}
704A-4[a]	1093	140	>1000	0.16	1.9×10^{-11}
732-3	1093	140	>1000	0.14	1.1×10^{-10}
732-7	1093	140	>1000	0.13	8.0×10^{-11}
717-1	1093	150	394	0.20	–
732-4	1093	150	190	0.14	–
704B-2[a]	1093	150	18.1	0.12	–
730-8	1093	160	15.4	0.12	–
704B-1[a]	1093	160	1.45	0.10	–
732-5	1204	125	>1000	0.25	3.0×10^{-11}
704B-5[a]	1204	125	>1000	0.20	8.0×10^{-11}
732-1	1204	140	>1000	0.31	2.3×10^{-10}
732-8	1204	140	454	0.28	–
732-6	1204	150	82.1	0.29	–
704A-5[a]	1204	150	0.32	0.18	-

[a] Panel 704 samples were slightly warped, possibly contributing to the relatively low fatigue lives.
§ A value of >1000 indicates a run-out, e.g. the sample survived the full 1000 hours without rupture.
* Strain at failure or strain at 1000 hr if sample was a run-out.

quantify the extent of the local creep-induced material degradation. While the work of Chermant et al. [13] provides a good insight into the mechanisms responsible for creep deformation and rupture in SiC/SiC CMCs, no attempt was made to develop a continuum-type creep material model which can be used within a finite element computational framework to analyze the performance and durability of CMC components operating under aggressive high-temperature high-stress conditions such as those encountered in gas-turbine engines. An example of the experimental results pertaining to the effect of temperature and stress on the temporal evolution of the creep strain as reported in Ref. [13] is depicted in Figure 4. Close examination of the results depicted in this figure reveals that the transition from the primary to secondary creep takes place at a time around 20 hours, and this transition time is not a sensitive function of either the temperature or stress.

Grujicic et al. [14] employed simulations to study the degradation of the mechanical properties of CMCs during creep. This degradation is caused by the fact that the CMC constituents possess different creep tendencies, and in order for them to acquire a common creep rate, undesirable load transfer typically occurs between fibers and the matrix. As a result, for the case of the SiC/SiC CMCs in which the matrix possesses superior creep resistance due to a larger grain size and high degree of stoichiometry and crystallinity, the first matrix-cracking stress (a measure of the CMC strength) is lowered [15]. In addition, if the reduction in the CMC strength is large enough to cause material cracking, stiffness degradation ensues [16]. The results obtained are used to enrich the SiC/SiC CMC material constitutive model suitable for the analysis of the response of this material under monotonic-loading conditions [17]. In other words, the effect of creep-induced material degradation was incorporated into the material constitutive model. However, the model was of a time-invariant character, and hence, it is not suitable for modeling either creep deformation or creep rupture.
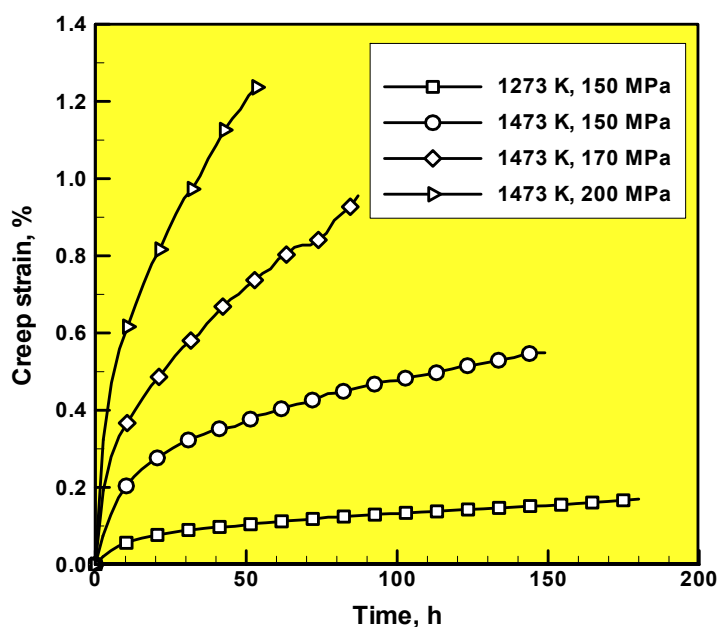

Figure 4. Evolution of creep strain with temperature and stress. (Data taken from Ref. [13].) Please see text in Section 2.1.3 for details regarding the architecture, constituent volume fraction, processing routes, and test procedures used in Ref. [13].

1.5. Main objective

The main objective of this work is to formulate, parameterize and validate the material models for: (a) creep-deformation; and (b) creep-rupture of SiC/SiC-based CMCs, subjected to multiaxial loading. The models to be developed will be implemented in a material user subroutine, coupled with a commercial finite element solver, and used in a finite element analysis of a prototypical gas-turbine engine creep deformation problem, i.e. creep-induced undesirable contact of a turbine-blade tip with the shroud.

1.6. Paper organization

In Section 2, the creep-deformation and creep-rupture models are formulated, parameterized and validated. A brief overview of the preliminary finite-element procedure used and the results obtained for the problem of turbine-blade tip contact with the shroud is presented in Section 3. A summary of the main conclusions of the study is given in Section 4.

2. CMC Creep-Models Development

In this section, the formulation, parameterization and validation of the creep-deformation and creep-rupture material models for SiC/SiC CMCs are described. For clarity, the two models are presented separately.

2.1. Creep-deformation material-model

Judging by the documented evolution of creep strain, Figure 4, the time of transition from the primary to the secondary creep regimes, t^*, has little dependence on the test temperature or applied stress. For simplicity, t^* is assumed to be constant and set to its average value of 20 h. Because studies have shown that the third stage of creep is generally not observed in SiC/SiC CMCs [13], first a time-dependent creep-deformation model for the primary-creep regime is developed, and then the creep-strain-rate predicted by this model at t^* is used as a measure of the steady-state creep rate. In other words, the primary-creep regime is modeled from first principles, but the second stage of creep is not modeled separately from the first stage.

2.1.1. Creep-Deformation Material-Model Formulation

For an isotropic material undergoing creep under uniaxial-stress σ, the primary-creep time-dependent axial-strain rate $\dot{\varepsilon}^{cr}$ is generally represented by this function:

$$\dot{\varepsilon}^{cr} = A\, e^{-Q/RT} \left(\frac{\sigma}{\sigma_0} \right)^n t^m \tag{1}$$

where A, Q (the activation energy), σ_0, m and n are material-specific parameters, R is the universal gas constant, T is the absolute temperature, and t is the time.

Eq. (1) is expanded for an isotropic material in a multidimensional creep-strain state, which results from multiaxial loading, as:

$$\dot{\bar{\varepsilon}}^{cr} = A\, e^{-Q/RT} \left(\frac{q}{\sigma_0}\right)^n t^m \tag{2}$$

where $\dot{\bar{\varepsilon}}^{cr}$ is the equivalent creep strain rate defined as

$$\dot{\bar{\varepsilon}}^{cr}\left(\dot{\mathbf{\varepsilon}}^{cr}\right) = \sqrt{\frac{2}{3}\dot{\mathbf{\varepsilon}}^{cr} : \dot{\mathbf{\varepsilon}}^{cr}}$$

$$\tag{3}$$

Time integration of Eq. (2) yields

$$\varepsilon^{cr} = A\, e^{-Q/RT} \left(\frac{q}{\sigma_0}\right)^n \frac{t^{m+1}}{m+1} \tag{4}$$

and the equivalent stress q is given by the von Mises relation:

$$q(\mathbf{\sigma}) = \sqrt{\frac{1}{2}\left[(\sigma_{22} - \sigma_{33})^2 + (\sigma_{33} - \sigma_{11})^2 + (\sigma_{11} - \sigma_{22})^2 + 6\left(\sigma_{23}^2 + \sigma_{31}^2 + \sigma_{12}^2\right)\right]} \tag{5}$$

(Boldface symbols are used to denote second-order tensorial quantities, while the : is used to denote an inner-product operator.)

Eq. (2) is still generally accepted for orthotropic materials, or more specifically transversely isotropic materials like CMCs, but $\dot{\bar{\varepsilon}}_{cr}$ and q are redefined to account for the reduced degree of material isotropy. For the CMCs analyzed here, the von Mises equivalent stress is replaced with the Hill's potential in the form:

$$q(\mathbf{\sigma}) = \sqrt{F(\sigma_{22} - \sigma_{33})^2 + G(\sigma_{33} - \sigma_{11})^2 + H(\sigma_{11} - \sigma_{22})^2 + 2L\sigma_{23}^2 + 2M\sigma_{31}^2 + 2N\sigma_{12}^2} \tag{6}$$

where the non-dimensional constants F, G, H, L, M, and N are functions of the uniaxial and pure-shear material strengths, and are determined from three uniaxial-tensile tests and three pure-shear tests (each associated with a unique material direction/plane). If a nominal strength measure σ^0 is introduced and the ratios of the six individual material strengths ($\bar{\sigma}_{ij}$) and σ^0 are defined as

$$R_{11} = \frac{\bar{\sigma}_{11}}{\sigma^0}, \ R_{22} = \frac{\bar{\sigma}_{22}}{\sigma^0}, \ R_{33} = \frac{\bar{\sigma}_{33}}{\sigma^0}, \ R_{23} = \frac{\bar{\sigma}_{23}}{\sigma^0/\sqrt{3}}, \ R_{31} = \frac{\bar{\sigma}_{31}}{\sigma^0/\sqrt{3}}, \ \text{and} \ R_{12} = \frac{\bar{\sigma}_{12}}{\sigma^0/\sqrt{3}}, \ \text{then the Hill's}$$

equivalent stress potential becomes:

$$q(\boldsymbol{\sigma}) = \left[\begin{array}{l} \dfrac{1}{2}\left(\dfrac{1}{R_{22}^2}+\dfrac{1}{R_{33}^2}-\dfrac{1}{R_{11}^2}\right)(\sigma_{22}-\sigma_{33})^2 + \dfrac{1}{2}\left(\dfrac{1}{R_{33}^2}+\dfrac{1}{R_{11}^2}-\dfrac{1}{R_{22}^2}\right)(\sigma_{33}-\sigma_{11})^2 \\[12pt] +\dfrac{1}{2}\left(\dfrac{1}{R_{11}^2}+\dfrac{1}{R_{22}^2}-\dfrac{1}{R_{33}^2}\right)(\sigma_{11}-\sigma_{22})^2 \\[12pt] +\dfrac{3}{R_{23}^2}\sigma_{23}^2 + \dfrac{3}{R_{31}^2}\sigma_{31}^2 + \dfrac{3}{R_{12}^2}\sigma_{12}^2 \end{array} \right]^{1/2} \tag{7}$$

Because a CMC is transversely isotropic and has a unique material direction x_3, $R_{11} = R_{22}$ and $R_{23} = R_{31}$, so that only four independent strength ratios are required. In addition, the material isotropy in the x_1-x_2 plane implies that q is invariant for a rotation about the x_3-axis, so R_{12} can be shown to be a function of the other strength ratios: $R_{12} = \sqrt{\dfrac{3}{\left(\dfrac{3}{R_{22}^2}+\dfrac{1}{R_{11}^2}-\dfrac{1}{R_{33}^2}\right)}}$. Therefore, a transversely isotropic material has only three independent strength ratios (R_{11}, R_{33}, R_{23}) and, if σ^0 is set to $\bar{\sigma}_{11}$, then $R_{11} = 1$.

The functional form of the equivalent creep-strain rate for a transversely-isotropic material is constructed by employing the work-rate equivalency as:

$$\frac{1}{2}\boldsymbol{\sigma} : \dot{\boldsymbol{\varepsilon}}^{cr} = \frac{1}{2}\bar{q} \cdot \dot{\bar{\varepsilon}}^{cr} \tag{8}$$

This procedure results in the following general functional form:

$$\dot{\bar{\varepsilon}}^{cr}\left(\dot{\boldsymbol{\varepsilon}}^{cr}, \boldsymbol{\sigma}, R_{11}, R_{33}, R_{23}\right) = \sqrt{f\left(\boldsymbol{\sigma}, R_{11}, R_{33}, R_{23}\right)\dot{\boldsymbol{\varepsilon}}^{cr} : \dot{\boldsymbol{\varepsilon}}^{cr}} \tag{9}$$

Given Eq. (2) and considering that a transversely isotropic material has three unique strength ratios, seven material-dependent parameters – A, Q, n, m, R_{11}, R_{33} and R_{23} – must be specified to completely define a first-stage (time-dependent) creep-deformation law for such a material. (Please note that σ^0 is not counted as a material parameter and is set arbitrarily to 1 MPa. However, it should be recognized that the value chosen for σ^0 affects the value of the material parameter A.) These parameters will be evaluated using experimental results [13] (reproduced in Figure 4), according to the procedure described in Section 2.1.2. The formulated and parameterized model will be validated against experimental results [13,1], as described in Section 2.1.3.

It should be noted that within the creep deformation model, as well as within the creep-rupture model, CMCs are treated as fully-homogenized, transversely isotropic materials. In other words, the main constituents of the CMCs (i.e. the matrix, the fibers, the fiber-coating and inter-constituent

interfaces) are recognized only implicitly. Thus, each material point contains a fixed volume fraction of its constituents, and their local orientation defines the local principal material directions. Clearly, as a result of the employed homogenization procedure, some fine details of the CMC mechanical response derived from the presence of the discrete constituents are lost. However, one must accept these types of shortcomings of the materials modeled when the ultimate goal is the use of such models in large-scale finite-element-based computational analyses of the performance and reliability of engineering components (like the ones encountered in gas-turbine engines).

2.1.2. Creep-deformation material-model parameterization

The primary-creep-evolution data, Figure 4, are used to parameterize the creep-deformation material model. While these creep-strain data pertain only to the strain component in the direction of the applied uniaxial stress, Eq. (4) requires the equivalent creep strain, and therefore the knowledge of the lateral creep strains. To obtain this data, first the two plastic Poisson's ratios ν_{12}^p and ν_{13}^p are computed using these conditions: (i) $\nu_{12}^p + \nu_{13}^p = 1.0$ (the volume constancy condition); and (ii) $\nu_{12}^p R_{22} = \nu_{13}^p R_{33}$ (the lateral strain scales inversely with the corresponding material strength). The corresponding lateral creep strains are computed from these Poisson's ratios as $\varepsilon_{22}^{cr} = -\nu_{12}^p \varepsilon_{11}^{cr} = -\dfrac{1}{1 + R_{11}/R_{33}} \varepsilon_{11}^{cr}$ and as $\varepsilon_{33}^{cr} = -\nu_{13}^p \varepsilon_{11}^{cr} = -\dfrac{1}{1 + R_{33}/R_{11}} \varepsilon_{11}^{cr}$. The two lateral-creep rates are related to the axial-creep rate by an analogous equation, and R_{11} can be set to 1.0 without loss of generality.

Once the three strength ratios are guessed or assumed for a given axial-creep stress, the corresponding equivalent creep strain can be determined using the integrated form of Eq. (9), provided the functional form for $f(\boldsymbol{\sigma}, R_{11}, R_{33}, R_{23})$ is known. To determine this functional form for the special case of uniaxial-stress loading in the x_1-direction, Eq. (8) is first invoked in conjunction with Eq. (7) to yield $\dot{\bar{\varepsilon}}^{cr} = \dot{\varepsilon}_{11}^{cr} R_{11}$ or upon integration, $\bar{\varepsilon}^{cr} = \varepsilon_{11}^{cr} R_{11}$. By writing the left-hand side of Eq. (9) as $\dot{\varepsilon}_{11}^{cr} R_{11}$, and substituting for the creep-strain components on the right-hand side of Eq. (9)

as: $\quad \dot{\varepsilon}_{22}^{cr} = -\dfrac{1}{1 + R_{11}/R_{33}} \dot{\varepsilon}_{11}^{cr}$, $\quad \dot{\varepsilon}_{33}^{cr} = -\dfrac{1}{1 + R_{33}/R_{11}} \dot{\varepsilon}_{11}^{cr}$ and $\quad \dot{\varepsilon}_{12}^{cr} = \dot{\varepsilon}_{23}^{cr} = \dot{\varepsilon}_{13}^{cr} = 0$, we obtain

$$f(\boldsymbol{\sigma}, R_{11}, R_{33}, R_{23}) = \frac{(R_{11})^2}{1 + (\nu_{12}^p)^2 + (\nu_{13}^p)^2} = \frac{(R_{11})^2}{1 + \left(\dfrac{1}{1 + R_{11}/R_{33}}\right)^2 + \left(\dfrac{1}{1 + R_{33}/R_{11}}\right)^2}$$. For an isotropic material,

$R_{11} = R_{33} = 1.0$ and the expression evaluates to $f(\boldsymbol{\sigma}, R_{11}, R_{33}, R_{23}) = 2/3$ as expected.

The three strength ratios are set separately from the other model parameters:

(i) R_{11} is set to 1.0;

(ii) since the relationship between the equivalent creep rate and uniaxial creep rate does not involve R_{33}, the uniaxial-creep data cannot be used to obtain R_{33}. This parameter is evaluated separately at the end; and

(iii) since the creep data given in Figure 4 do not involve any shear component of the creep strain, these data cannot be directly used to obtain R_{23}. This parameter is also evaluated later.

The remaining four parameters (A, Q, n and m) in the primary-creep-deformation model for SiC/SiC CMCs are determined using a constrained single-objective-function optimization procedure, with the parameters treated as design variables. The constraints on the parameters are that all of them should be positive (so that the equivalent creep strain is positive), except m, which should be negative (so that the primary creep-deformation rate decreases over time).

The objective function to be minimized can be written in the following general form:

$$\text{obj\_func} = \sum_I \sum_i \left[\varepsilon_{I,i}^{cr} - A \, e^{-Q/RT_I} \left(\frac{q_I(\boldsymbol{\sigma}, R_{11}, R_{33}, R_{23})}{\sigma_0} \right)^n \frac{t_I^{m+1}}{m+1} \right]^2 \tag{10}$$

where summation index $I = 1-4$ and corresponds to the four temperature/axial-stress combinations given in Figure 4, while the summation index $i = 1-9$ corresponds to the data points in the primary-creep section of each curve in this figure.

Using this procedure, the optimal values of the four primary-creep SiC/SiC CMC material-model parameters are obtained as: $A = 1.169 \cdot 10^{-10} \quad 1/s^{0.4672}$, $Q = 99.492 \, \text{kJ/mol}$, $n = 3.8147$ and $m = -0.5328$. The remaining model parameters appearing in Eq. (10) are set as follows: (a) $R_{11} = 1.0$;

(b) $R_{33} = R_{11} \cdot (\bar{\sigma}_{33}/\bar{\sigma}_{11}) = 1.0 \cdot 0.54 = 0.54$, where the through-the-thickness to in-plane strength ratio is assumed to be 0.54, a typical value; (c) $R_{23} = R_{12} = \sqrt{\dfrac{3}{\left(\dfrac{3}{R_{22}^2} + \dfrac{1}{R_{11}^2} - \dfrac{1}{R_{33}^2} \right)}} = 2.29$; and (d)

$\sigma^0 = 1.0 \, \text{MPa}$. It should be noted that the assigned values for these four parameters will not affect the outcome of the material-model validation presented in the next subsection. However, R_{33} and R_{23} may have some effect on the results obtained in the last part of this study, which deals with the creep-deformation response of a gas-turbine engine blade.

2.1.3. Creep-deformation material-model validation

The formulated and parameterized primary-creep-deformation model has been validated in two steps:

(a) In the first step, the "goodness of fit" is assessed by comparing the equivalent creep-strain data obtained "experimentally" ($\varepsilon_{I,i}^{cr}$ in Eq. (10)) and computationally ($A\,e^{-Q/RT_I}\left(\dfrac{q_I}{\sigma_0}\right)^n \dfrac{t_I^{m+1}}{m+1}$, also in Eq. (10)) for the same conditions of temperature, axial stress and time. This comparison is illustrated using the $y = A\,e^{-Q/RT_I}\left(\dfrac{q_I}{\sigma_0}\right)^n \dfrac{t_I^{m+1}}{m+1}$ vs. $x = \varepsilon_{I,i}^{cr}$ correlation plot shown in Figure 5(a). The line shown for $y = 0.995x - 3.565 \cdot 10^{-5}$ was obtained using linear regression, suggesting that the parameter-identification procedure employed was quite successful in accounting for the measured primary-creep behavior of the SiC/SiC CMCs.

The goodness of fit is further quantified using the distribution of the relative error (defined as the difference between the calculated and experimental equivalent creep strain divided by the half-sum of these strains, and calculated from the non-zero equivalent creep strain data shown in Figure 5(a)), as shown in Figure 5(b). Since the magnitude of the relative error is less than 3.5% for 28 out of 32 (nonzero creep-strain) data points, the parameter-evaluation procedure can be considered as reasonably successful; and

(b) In the second step, the model predictions for the steady-state equivalent creep rate are compared with experimental data that was not used to evaluate the parameters. The model predictions of steady-state equivalent creep-rate are evaluated using Eq. (2), with $t^* = 20\,\text{h}$ and the parameters set to their optimal values. The experimental steady-state equivalent creep-rates are evaluated using the data provided in Refs. [13,1]. Because Ref. [13] gives uniaxial creep strain vs. time data (reproduced in Figure 4) in the steady creep-deformation regime, $t^* > 20\,\text{h}$, the slope of each set of steady creep-deformation data (determined from linear regression) is used as a measure of the corresponding average uniaxial steady-state creep rate. Ref. [1] directly provides uniaxial-creep rates (reproduced in Table 1) for the four test conditions corresponding to the full factorial design of experiments, with two levels of temperature ($T = 1093^0\text{C}$ and $T = 1204^0\text{C}$) and two levels of uniaxial stress ($\sigma = 125\,\text{MPa}$ and $\sigma = 140\,\text{MPa}$), and a creep run-out time of 1000 hours. The uniaxial steady-state creep-rate data obtained from both Refs. [13] and [1] are converted to their corresponding equivalent steady-state creep rates using the procedure explained above.

To assess the success of the time-dependent creep-deformation model in accounting for the observed steady-state creep behavior of the SiC/SiC CMCs, the measured equivalent steady-state creep rates, $\dot{\varepsilon}_{\text{steady,exper}}^{cr}$ (evaluated from the experimental creep-strain data [13] reproduced in Figure 4) and the corresponding model predictions, $\dot{\varepsilon}_{\text{steady,model}}^{cr}$, are shown in a correlation plot in Figure 6(a). It should be noted that the measured equivalent steady-state creep-rate data from Ref. [13] used in this

portion of the work were not employed in the material-model parameterization discussed earlier. Thus, the results presented in Figure 6(a) can be used to judge the predictive capacity of the material creep-deformation model, at least for the CMC investigated in Ref. [13]. It should be further noted that the experimental creep-rate data reported in Ref. [1] are not shown in Figure 6(a) since they are one to two orders of magnitude lower than those obtained in Ref. [13], and would cluster at the origin of this linear-linear plot. The line $y = 1.29x + 6.28 \cdot 10^{-9}$ is obtained using linear regression, suggesting that using the primary-creep equivalent rate at $t^* = 20\,\text{h}$ as a measure of the steady-state creep rate yields reasonable predictions when compared to the experimental data in Ref. [13].

To visualize data from Refs. [13] and [1] together, the correlation plot and line are redrawn using a logarithmic scale in Figure 6(b), with the steady-state creep-rate data from Ref. [1] superposed. The creep-deformation material model is observed to be less successful in accounting for the steady-state creep-rate data reported in Ref. [1]. Differences between the studies may account for this discrepancy, the main ones being:

(a) In Ref. [13], the SiC-matrix was processed via CVI, resulting in a microstructure that was more finely-grained, and so more creep-prone. In Ref. [1], the SiC-matrix was fabricated using molten-silicon infiltration [e.g. 20, 21], resulting in a microstructure that was more coarsely-grained, and so more creep-resistant;

(b) Although CMCs used in both studies contained Hi-Nicalon fibers, the fiber coating consisted of a layer of pyrolitic carbon having unspecified thickness in Ref. [13], but consisted of four layers (BN/C/Si_3N_4/C) the thicknesses of which were carefully controlled in Ref. [1];

(c) The volume fraction of the fibers was not specified in Ref. [13], but was specified as 32 vol.% in Ref. [1];

(d) In Ref. [13], CMCs possessed a 2.5-D ply architecture, while in Ref. [1] the CMC had a cross-ply architecture; and

(e) The two studies employed significantly different experimental apparatus, and specimens having significantly different geometries and sizes, for the creep-tests.

Given the aforementioned differences in the architectures, constituent volume fractions, processing routes, and test procedures used in Refs. [13] and [1], it is not surprising that the present CMC creep-deformation material model is not very successful in accounting for the creep-deformation behavior of the CMCs used in Ref. [1]. This finding suggests that the present CMC creep-deformation material model should be reparameterized for the CMCs employed in Ref. [1]. Unfortunately, the experimental data reported in Ref. [1] is not sufficient to carry out a complete and reliable reparameterization of the creep-deformation material model.

It should be noted that the lack of portability of the present creep-deformation material model across the CMCs with different architectures, constituent volume fractions, and processing routes can be addressed by analyzing the CMC creep-deformation process using a micromechanics modeling and computation framework. Within this approach, CMC constituents are modeled explicitly. While the use of a micromechanics approach is beyond the scope of the present work, its utility will be investigated in our future work.

The results of the validation procedure suggest that:

(i) once creep-behavior data for a particular CMC under given conditions are used to parameterize the creep-deformation material model, it can be employed to predict the creep behavior of the same CMC under other conditions, with relatively high accuracy; and

(ii) the model predictions are less accurate for a similar grade of CMC, having different fiber- and ply-level architectures, processed by a different route and tested under different conditions. This finding is fully justified since the microstructure, and so the properties (including the creep-deformation behavior) of the CMCs have been shown to strongly depend on the architectures and processing routes [1].

2.2. Creep-rupture material-model

As in the case of the creep-deformation model, development of the creep-rupture model involves three separate steps: (i) formulation; (ii) parameterization; and (iii) validation.

2.2.1. Creep-Rupture Material-Model Formulation

In this study, the typical approach is taken to formulating a creep-rupture material model: a functional form is used which relates the rupture-time to the applied stress and temperature. The functional form, Eq. (11), is related to that for the steady-state creep-rate:

$$\tau_r = A_r\, e^{Q_r/RT} \left(\frac{q}{\sigma_0} \right)^{n_r} \tag{11}$$

where subscript r is used to denote creep-rupture material-model parameters, and q again denotes the Hill's potential as given by Eq. (6).

Given Eq. (11) and recognizing that the strength ratios R_{11}, R_{33} and R_{23} were already determined, and that σ^0 was set to 1 MPa, the complete definition of the creep-rupture model involves specifying three additional parameters: A_r, Q_r and n_r. In Section 2.2.2, a procedure will be described to evaluate these parameters using the experimental results (for the effect of the applied uniaxial-stress and temperature on the rupture-time) reported in Ref. [13] and reproduced in Figure 4. In Section 2.2.3, a procedure will be described to validate the formulated and parameterized model against the experimental results reported in Ref. [1].
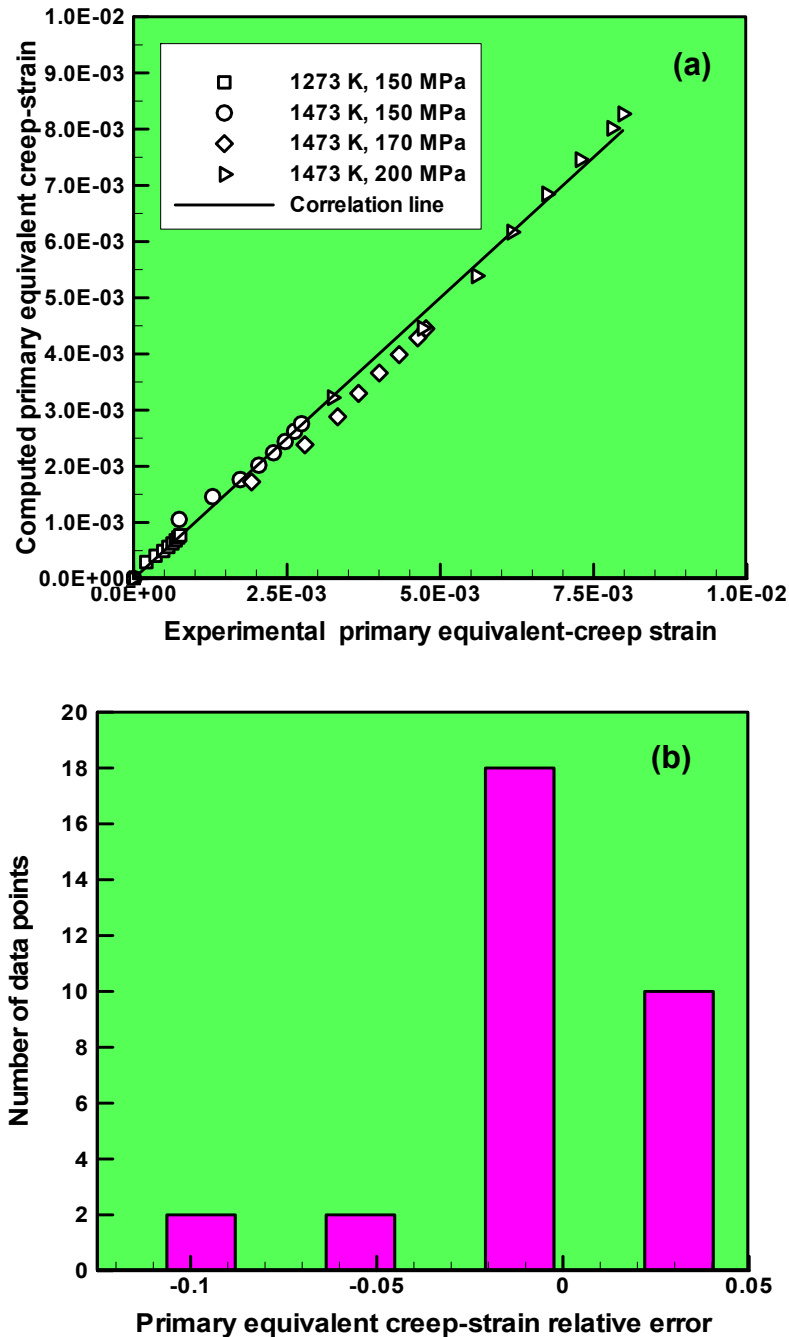
Figure 5. (a) Correlation plot of primary equivalent creep-strain data from experiments [13] and computations, for the same conditions of temperature, axial stress and time, with the regression line $y = 0.995x - 3.565 \cdot 10^{-5}$; and (b) distribution of the relative error in primary equivalent creep-strain.
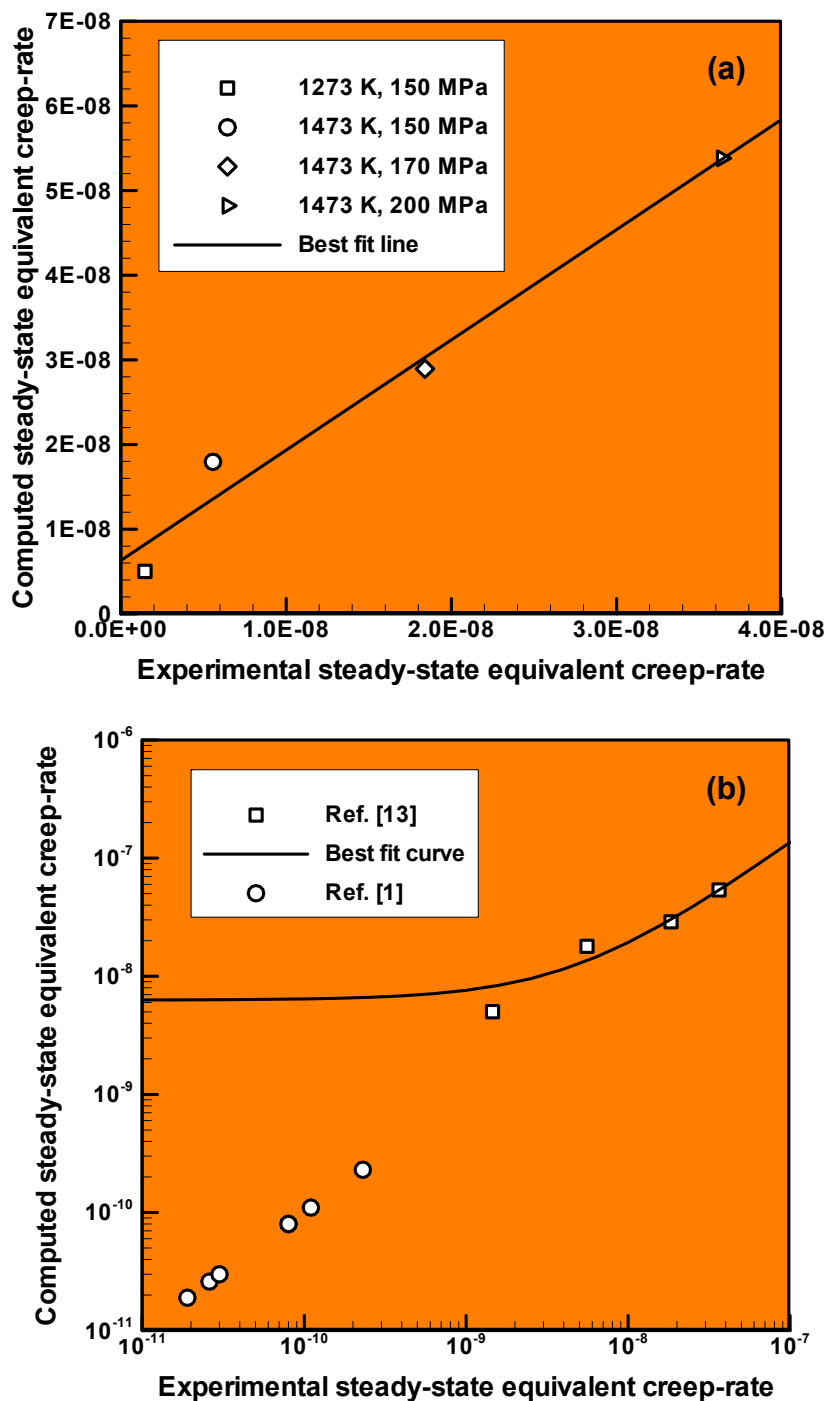
Figure 6. (a) Correlation plot of steady-state equivalent creep-rate data from experiments [13] and computations, with regression line $y = 1.29x + 6.28 \cdot 10^{-9}$; and (b) correlation plot redrawn using a logarithmic scale, with the steady-state equivalent creep-rate data from Ref. [1] superposed. Please see text in Section 2.1.3 for differences in the architecture, constituent volume fraction, processing routes, and test procedures used in Refs. [13] and [1], which can account for the observed differences in the creep behavior.

2.2.2. Creep-Rupture Material-Model Parameterization

The results for the creep-rupture time, Figure 4, are used to parameterize the creep-rupture model for SiC/SiC CMCs. The remaining three material parameters (A_r, Q_r and n_r) in the model are determined using a constrained single-objective-function optimization procedure in which the parameters act as design variables. The constraints imposed on the parameters are that A_r and Q_r should be positive (so that the rupture time is positive) while n_r should be negative (so that the rupture-time decreases as the applied stress increases).

The objective function to be minimized can be written in the general form:

$$\text{obj\_func} = \sum_I \left[\tau_{r,I} - A_r \; e^{Q_r/RT_I} \left(\frac{q_I(\boldsymbol{\sigma}, R_{11}, R_{33}, R_{23})}{\sigma_0} \right)^{n_r} \right]^2 \tag{12}$$

where summation index $I = 1 - 4$ and corresponds to the four temperature/axial-stress combinations given in Figure 4.

This procedure yields the optimal values of the three creep-rupture material-model parameters as: $A_r = 7.57 \cdot 10^5 \text{ h}$, $Q_r = 95.007 \text{ kJ/mol}$, and $n_r = -3.26$. The activation energy calculated for the creep-rupture process (95.007 kJ/mol) is quite comparable to the activation energy for the creep deformation process ($Q = 99.492 \text{ kJ/mol}$).

2.2.3. Creep-Rupture Material-Model Validation

The creep-rupture model is validated in two steps (as was the primary-creep-deformation model):

(a) In the first step, the "goodness of fit" is assessed by comparing the "experimental" creep-rupture times taken from Figure 4 (the data used in the material-model parameterization) against the model predictions. The outcome of this procedure is shown as a correlation plot in Figure 7(a). The line $y = 1.0012x - 2.43 \; (\text{h})$ was obtained using linear regression, suggesting that the parameter-identification procedure employed was quite successful in accounting for the measured creep-rupture time of the SiC/SiC CMCs; and

(b) In the second step, the model predictions for the rupture time are compared with experimental data (from Ref. [1], as reproduced in Table 1) that was not used to evaluate the parameters. Specifically, eight data points from Table 1 are used, pertaining to rupture-times shorter than the creep-runout time of 1000 hours; these points correspond to four different temperature-stress conditions. The results of this comparison are shown as an eight-point scatter plot in Figure 7(b); the experimental creep-rupture times (taken from Table 1) are plotted along the x-axis and the corresponding model predictions (as given by Eq. (11)) along the y-axis. The line shown corresponds

to perfect experiment/model correlation (i.e. a line with a slope of 1.0 and an intercept of 0.0). The creep-rupture material model is observed to be not very successful in accounting for the measured creep-rupture times, as reported in Ref. [1]. This finding again is not surprising, considering that: (i) the creep-rupture times measured in experiments under identical temperature-stress conditions could differ by as much as one to two orders of magnitude [1]; and (ii) like the steady-state creep rate, the creep-rupture time is expected to depend on the CMC architecture, material microstructure and processing route, which are substantially different for the CMCs used in Refs. [13] and [1].

Given the aforementioned differences in the CMC architectures, constituent volume fractions, and processing routes used in Refs. [13] and [1], it is again not surprising that the present CMC creep-rupture material model is not very successful in accounting for the creep-rupture behavior of the CMCs used in Ref. [1]. This finding suggests that the present CMC creep-rupture material model should be reparameterized for the CMCs employed in Ref. [1]. Unfortunately, the experimental data reported in Ref. [1] is not sufficient to carry out a complete and reliable reparameterization of the creep-rupture material model.

It should also be noted that the CMC creep-rupture process is of a stochastic character and is not purely deterministic, as assumed in the present work. In other words, the creep-rupture model should not predict a fixed rupture-time for a given combination of the imposed temperature and stress. Instead, the model should predict that the component will be able to survive exposure of a specified duration, with a given level of probability, to the imposed temperature and stress conditions. While the present (deterministic) creep-rupture material model can be readily made stochastic, a lack of detailed experimental data would prevent parameterization of such a stochastic creep-rupture material model. That is the main reason that the creep-rupture process, and the associated material model, are considered to be of a deterministic character in the present work.

3. Application of the Creep Models to a Turbine Blade

While the main objective of the present work was development, parameterization and validation of the creep-deformation and creep-rupture models for SiC/SiC CMCs under multi-axial loading conditions, the work is underway to link these models with a finite-element solver in order to be able to computationally study the problem of the engineering performance and durability of a gas-turbine engine component. A complete report of the results to be obtained in the ongoing work will be presented in a future communication. In this section, an example of the preliminary results obtained in the ongoing investigation is given for the use of the creep-deformation model within a finite-element-based computational analysis of the performance of a prototypical SiC/SiC CMC-blade located within the low-pressure section of a gas-turbine (aviation) engine.

3.1. A brief description of the problem

The performance of a prototypical blade located within the low-pressure section of a gas-turbine (aviation) engine is analyzed. The blade is attached to a high-speed (10,000 rpm) rotating shaft, with a small clearance (ca. 0.25 mm) between the blade-tip and shroud. A schematic of a blade attached to the hub and a single shroud-segment is depicted in Figure 8. In the course of normal operation, the combination of high temperatures and high centrifugal forces will cause the blade to creep outward (in the radial direction of the gas-turbine engine) and the blade-tip/shroud clearance to decrease and
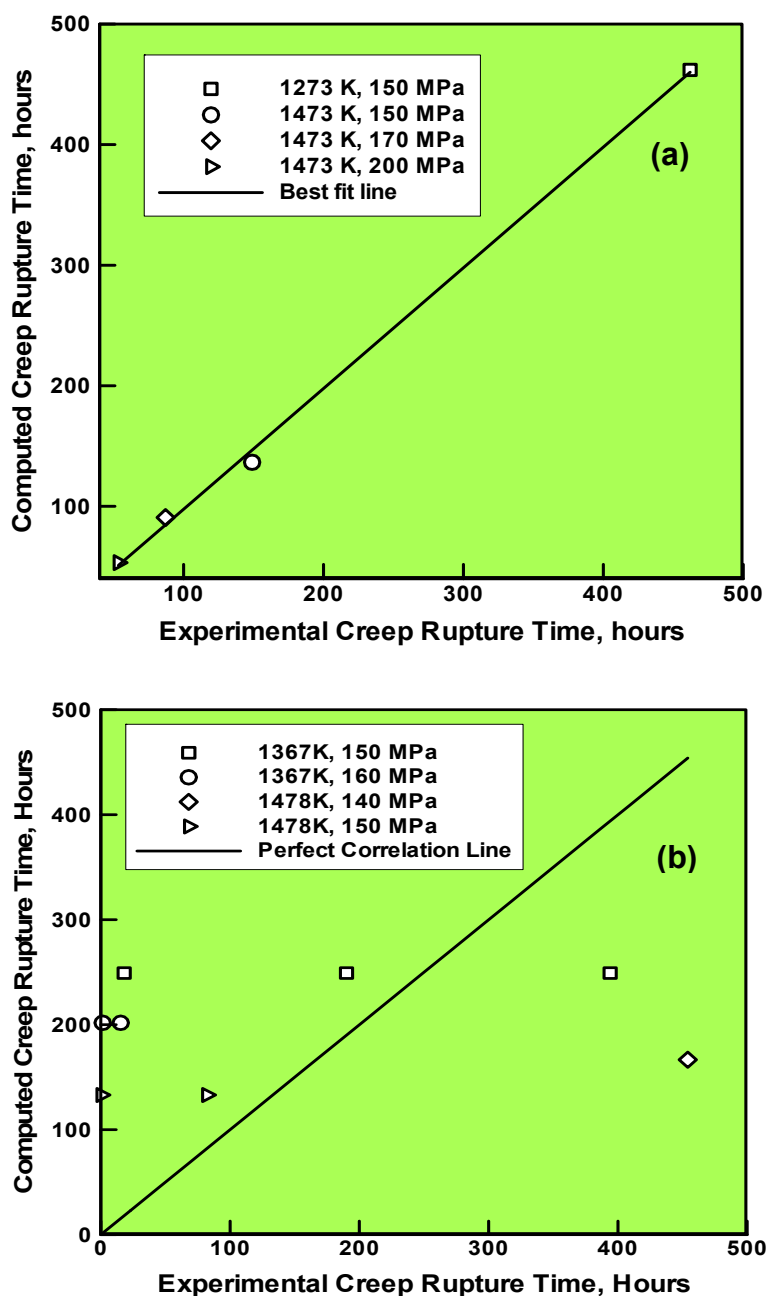
Figure 7. (a) Correlation plot of creep-rupture times from experimental data and computations, with regression line $y = 1.0012x - 2.43$ (h); and (b) comparison of creep-rupture time data from experiments (given in Table 1) and model predictions (as given by Eq. (11)). The line $y = x$ corresponds to perfect experiment/model correlation.

ultimately become zero. To prevent the resulting undesirable blade-tip rub of the shroud, the gas-turbine engine operation will have to be temporarily halted and the blade-tip trimmed (as needed). This procedure could be repeated a few times to extend the life of the blade. However, the extent of creep-deformation within the blade will eventually become excessive, particularly in the blade-root

region (i.e. in the region where the blade is attached to the hub), and the blade may rupture. Since blade rupture is not permitted, the rupture time of the blade material adjacent to the hub controls the useful life of the blade. The creep-deformation material model developed enables the prediction of the maintenance schedule of the gas-turbine engine, while the creep-rupture model can be used to predict the useful life of the blade. In the present work: (a) only a brief description of the finite-element procedure used will be given; and (b) selected preliminary finite-element results pertaining to the blade performance will be presented and discussed. In our future work, a detailed account of the finite-element procedure used will be given, as well as a more comprehensive set of results pertaining not only to the performance but also to the durability of the turbine blade.

3.2. Finite element analysis

In general, the following items should be specified for a prototypical finite element analysis of the performance of a structural component like a gas-turbine engine blade: (a) geometrical model; (b) meshed model; (c) computational algorithm; (d) initial conditions; (e) boundary conditions; (f) contact interactions; (g) material models; and (h) computational tool. These items are briefly discussed in the remainder of this subsection.

3.2.1. Geometrical model

As shown in Figure 8, the geometrical model employed consisted of three distinct components (the key dimensions of which are indicated): (a) hub; (b) blade; and (c) a single shroud-segment.

3.2.2. Meshed model

First-order four-node tetrahedron continuum elements were used to mesh each component, with the total number of elements in each component being: (a) hub – ca. 350,000; (b) blade – ca. 74,000; and (c) shroud-segment – ca. 3,500, and the average element-edge length being ca. 2 mm. The mesh size used was selected to achieve a tradeoff between computational accuracy and computational cost. The blade was attached to the hub by having the two components share nodes at the joint.

3.2.3. Computational algorithm

Two distinct static loading steps were simulated:

(a) an elastic step within which the hub and blade were subjected to the centrifugal distributed loading (with respect to the hub axis as the axis of rotation) associated with the hub rotation about its axis at an angular velocity of 10,000 rpm; and

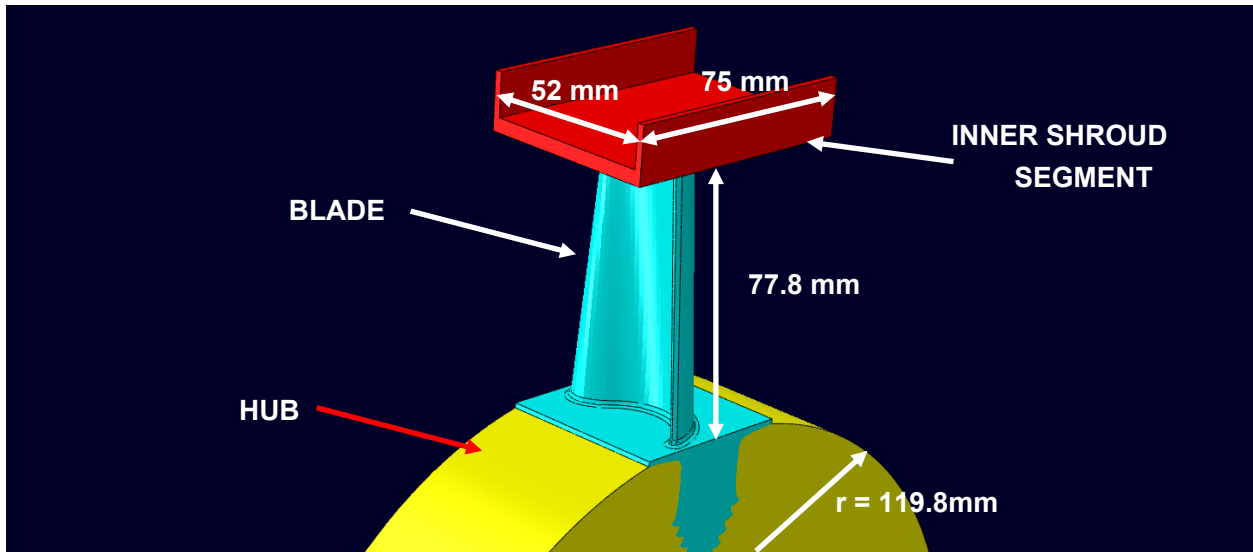(b) a visco-type loading step, within which allowance was made for the creep-deformation within the hub and blade.

Figure 8. Geometrical model employed in the present work, consisting of three distinct components: (a) hub; (b) blade; and (c) a single shroud-segment. Key dimensions of the three components are indicated.

3.2.4. Initial conditions

The blade, hub and shroud segment were all assumed to be stress-free at the beginning of the first loading step. The temperature was assumed uniform and constant (1473 K) throughout the computational model.

3.2.5. Boundary conditions

In the first loading step, a distributed centrifugal load was applied to the hub and blade, corresponding to the hub rotating about its axis at 10,000 rpm (the axis was not allowed to translate). The same loading was retained in the second step, during which the hub and blade were enabled to undergo time-dependent deformation (creep). As mentioned above, the temperature within the model was assumed to be uniform and constant throughout the analysis.

3.2.6. Contact Interactions

The "Hard Contact Pair" type of contact algorithm [18,19] was employed to model all normal interactions between the blade-tip and shroud-segment. Within this algorithm, contact pressures between two bodies were transmitted only if the nodes on the *slave surface* contacted the *master surface*. No penetration/overclosure between the slave and master surfaces was allowed, and there was no limit to the magnitude of the contact pressure that could be transmitted when the surfaces were in contact. Transmission of shear stresses across the contact interfaces was assumed to be controlled by a modified Coulomb friction law. This law utilizes a static, μ_{st}, and a kinetic, μ_{kin}, friction coefficient and an upper-bound shear stress limit, τ_{slip} (a maximum value of shear stress

which can be transmitted before shearing within the softer material, rather than interfacial sliding, begins to take place).

3.2.7. Material models

The hub was assumed to be made of GTD-111 (equiaxed), the blade of SiC/SiC CMC, and the shroud-segment of Inconel 718 (equiaxed). In the preliminary finite-element analysis, the constitutive models for all participating materials included elastic and creep components. However, results indicated that the GTD-111 (hub) and Inconel 718 (shroud) experience significantly less creep than the SiC/SiC CMC (blade). For this reason, only an elastic response was prescribed for GTD-111 and Inconel 718 in subsequent calculations. Given their equiaxed grain-size microstructures, both materials were treated as being isotropic linear-elastic, so that their constitutive models are fully defined by specifying the Young's modulus E and Poisson's ratio ν. The following values of E and ν were used: (a) GTD-111–170 GPa, 0.28; and (b) Inconel 718–203 GPa, 0.30. The constitutive response of the SiC/SiC CMC under high-temperature sustained loading was assumed to be appropriately accounted for by the creep-deformation model developed.

3.2.8. Computational Tool

ABAQUS/Standard, a general purpose finite-element program [22–25], was used for all calculations. The problem is solved using an implicit nonlinear static finite-element algorithm within which the mechanical equilibrium within the system is solved repeatedly as a function of time, since the mechanical equilibrium established at the end of the previous time increment is perturbed, by the operation of the creep-deformation processes, within the current time increment. A typical simulation run pertaining to the creep-deformation within the blade required 4 hours of (wall-clock) time on a 12-core, 3.0 GHz machine with 12 GB of memory.

3.3. Results and discussion

The distribution of the Hill's potential in the blade just before shroud/blade-tip contact is established is shown in Figure 9(a). (For clarity, the hub is not shown.) The distribution has the following features: (a) the Hill's potential is highest in the blade region adjacent to the blade/hub joint and tapers off towards the blade-tip; (b) since the hub shares the blade-borne centrifugal load at the rigid joint, the Hill's potential in the blade (i.e. axial stress due to centrifugal force) is lower at the joint; and (c) since the shroud segment is stationary and does not contact the blade, it exhibits a zero value of the Hill's potential.

The distribution of the Hill's potential in the blade immediately after shroud/blade-tip contact is established is shown in Figure 9(b). A comparison of this distribution to the one shown in Figure 9(a) indicates that: (a) variation of the Hill's potential through the blade is effectively the same before and after contact. If the contour levels are refined, some small differences are observed in the blade-tip region for the two cases. However, these differences vanish further away from the blade-tip; and (b) because it has been contacted by the blade-tip, the shroud segment now exhibits non-zero values of the Hill's potential (more precisely the von Mises potential, because the shroud material is isotropic). (Different ranges and contour levels of Hill's/von Mises potential are used for the blade and the

shroud, since the contact stresses observed are quite small compared to the centrifugal stresses experienced by the blade.)

The spatial distribution of equivalent creep strain in the blade at the moment when its tip first contacts the shroud (9763 hours of engine operation) is shown in Figure 10. The equivalent creep strains are observed to be highest in the region of the blade adjacent to the blade/hub joint, and gradually reduce towards the blade-tip. This distribution of the equivalent creep strain is expected given a similar distribution of Hill's equivalent potential (depicted in Figures 9(a)-(b)). Since the creep phenomenon was not modeled for the hub and the inner shroud material, these components are not shown in Figure 10.

The computational analysis showed that the blade-tip first contacted the shroud after 9763 hours under the assumed design and operating conditions: (a) blade-tip/shroud clearance of 0.25 mm; (b) operating temperature of 1473K; and (c) hub rotational speed of 10000 rpm. This finding suggests that, if the rotor is to be overhauled every 5000 hours, then the blade-tip/shroud clearance can be reduced to 0.128 mm. Doing so would improve gas-turbine engine efficiency by reducing the amount of combustion gases escaping around the blade-tip.
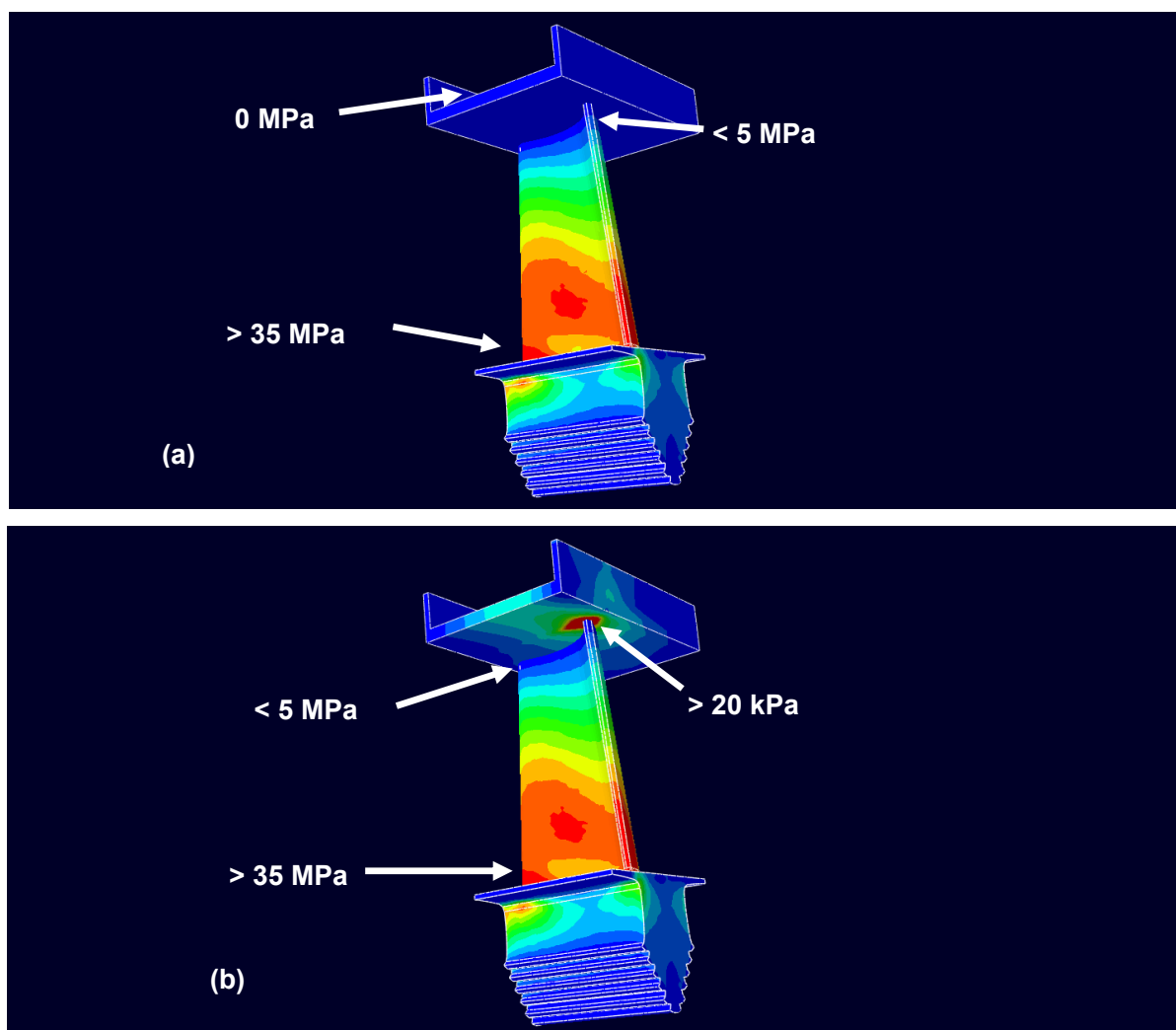

Figure 9. Spatial distribution of Hill's potential on the SiC/SiC CMC blade: (a) just prior to the blade-tip/inner shroud contact event; and (b) immediately after the blade-tip/inner shroud contact event.
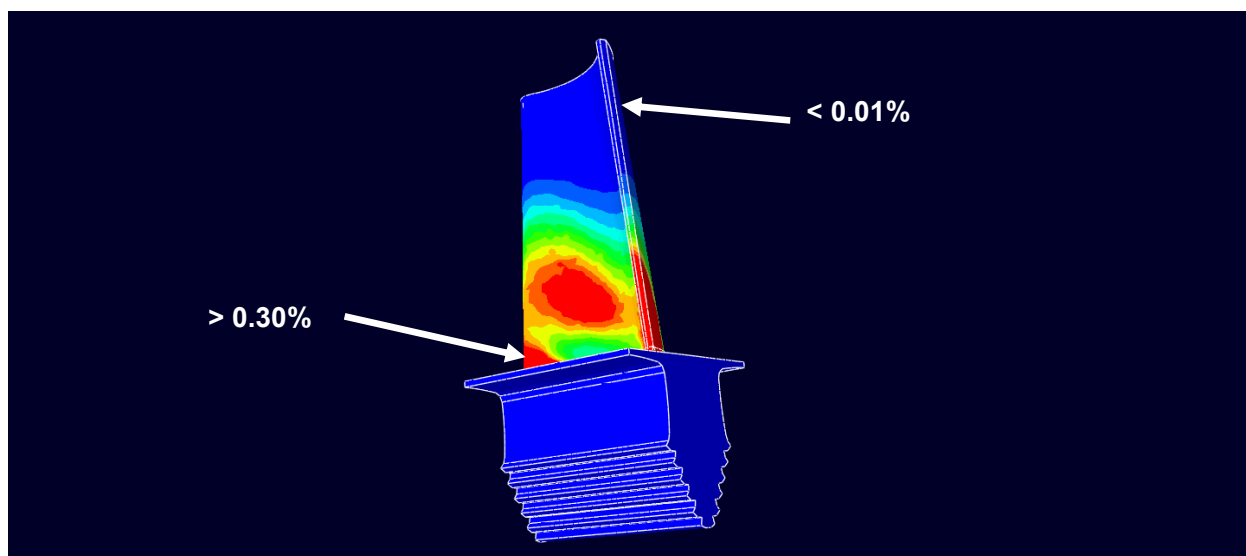
Figure 10. Spatial distribution of equivalent creep strain over the SiC/SiC CMC blade at the moment of first blade-tip/inner-shroud contact event (9763 hours of engine operation).

4. Conclusion

Based on the results obtained in the present work, the following main summary remarks and conclusions can be drawn:

1. Material constitutive models for creep deformation and creep rupture under general three-dimensional loading have been developed for SiC/SiC ceramic-matrix composites (CMCs), treated as transversely isotropic materials.

2. To parameterize the models, one set of experimental data reported in the literature has been employed. To validate the parameterized models, another set of experimental data also reported in the literature was used.

3. The results of the material-model validation revealed the effect that the details of the CMC-material processing route and microstructure have on the model parameterization. Specifically, the material model parameterized using experimental data for a CMC in which the matrix was fabricated by chemical vapor infiltration has been found not to be very reliable when applied to a CMC in which the matrix was fabricated using melt infiltration (even when the other aspects of the CMC fabrication and microstructure are quite comparable in the two renditions of this material).

4. In the last portion of the work, preliminary finite-element results pertaining to the performance of a CMC-blade located in the low-pressure stage of a gas-turbine engine are generated and used in order to demonstrate the utility of the creep-deformation model developed. Specifically, these results have been used to help establish the needed gas-turbine engine-maintenance schedule involving trimming of the blade-tip, in order to prevent the undesirable blade-tip/inner-shroud rub condition.

Conflict of Interest

All authors declare no conflicts of interest in this paper.

References

1. Corman GS, Luthra KL (2006) Melt Infiltrated Ceramic Composites (HIPERCOMP®) For Gas Turbine Engine Applications, Continuous Fiber Ceramic Composites Program Phase II Final Report, Niskayuna, NY: GE Global Research, Technical Report DOE/CE/41000-2.
2. CFM International, LEAP Engine. Available from http://www.cfmaeroengines.com/engines/leap, accessed December 1, 2015.
3. GE Aviation, GE Successfully Tests World's First Rotating Ceramic Matrix Composite Material for Next-Gen Combat Engine. Available from http://www.geaviation.com/press/military/military_20150210.html [accessed December 1, 2015].
4. Grujicic M, Galgalikar R, Snipes JS, et al. (2016) Creep-behavior-based material selection for a clamping spring of ceramic-matrix composite inner-shroud in utility and industrial gas-turbine engines. *J Mater Des Appl*.
5. Ashby MF, Abel CA (1995) Materials selection to resist creep. *P Roy Soc A* 351: 451–468.
6. Ashby MF, Shercliff HR, Cebon D (2007) Materials: Engineering, science, processing and design. Oxford, UK: Butterworth-Heinemann.
7. Morscher GN (2010) Tensile creep and rupture of 2-D woven SiC/SiC composites for high temperature applications. *J Eur Ceram Soc* 30: 2209–2221.
8. Morscher GN, Pujar VV (2006) Creep and stress-strain behavior after creep for SiC fiber reinforced, melt-infiltrated SiC matrix composites. *J Am Ceram Soc* 89: 1652–1658.
9. Morscher GN, Ojard G, Miller R, et al. (2008) Tensile creep and fatigue of Sylramic-iBN melt-infiltrated SiC matrix composites: Retained properties, damage development, and failure mechanisms, *Compos Sci Technol* 68: 3305–3313.
10. van Roode, Bhattacharya AK, Ferber MK, et al. (2010) Creep Resistance and Water Vapor Degradation of SiC/SiC Ceramic Matrix Composite Gas Turbine Hot Section Components, *Proceedings of ASME Turbo Expo 2010: Power for Land, Sea and Air GT2010, June 14-18, 2010, Glasgow, UK*.
11. Rospars C, Chermant JL, Ladevèze P (1998) On a first creep model for a 2D SiC$_f$–SiC composite. *Mater Sci Eng* 250: 264–269.
12. Rugg KL, Tressler RE, Bakis CE, et al. (1999) Creep of SiC-SiC Microcomposites. *J Eur Ceram Soc* 19: 2285–2296.
13. Chermant JL, Boitier G, Darzens S, et al., (2002) The creep mechanism of ceramic matrix composites at low temperature and stress, by a material science approach. *J Eur Ceram Soc* 22: 2443–2460.
14. Grujicic M, Galgalikar R, Snipes JS, et al. (2016) Multi-length-scale material model for SiC/SiC ceramic-matrix composites (CMCs): inclusion of in-service environmental effects. *J Mater Eng Perform* 25: 199–219.
15. Casas L, Martinez-Esnaola JM (2003) Modelling the effect of oxidation on the creep behaviour of fibre-reinforced ceramic matrix composites. *Acta Mater* 51: 3745–3757.
16. Takeda M, Imai Y, Ichikawa H, et al. (1999) Thermal stability of SiC fiber prepared by an irradiation curing process. *Compos Sci Technol* 59: 793–799.
17. Grujicic M, Snipes JS, Galgalikar R, et al. (2015) Multi-length-scale derivation of the room-temperature material constitutive model for SiC/SiC ceramic-matrix composites (CMCs). *J Mater: Des Appl* [in press].

18. Grujicic M, Chenna V, Galgalikar R, et al. (2014) Computational analysis of gear-box roller-bearing white-etch cracking: a multi-physics approach. *Inter J Struct Integrity* 5: 290–327.

19. Grujicic M, Ramaswami S, Yavari R, et al. (2016) Multi-physics computational analysis of white-etch cracking failure mode in wind-turbine gear-box bearings. *J Mater Des Appl* 230: 43–63.

20. Grujicic M, Galgalikar R, Ramaswami S, et al. (2015) Multi-Physics Modeling and Simulations of Reactive Melt Infiltration Process Used in Fabrication of Ceramic-Matrix Composites (CMCs). *Multidiscip Mod Mater Struct* 11: 43–74.

21. Grujicic M, Snipes JS, Yavari R, et al. (2015) Computational Investigation of Foreign Object Damage Sustained by Environmental Barrier Coatings (EBCs) and SiC/SiC Ceramic-Matrix Composites (CMCs*). Multidiscip Mod Mater Struct* 11: 238–272.

22. ABAQUS Version 6.14, (2014) User Documentation, Dassault Systèmes.

23. Grujicic M, Ramaswami S, Snipes JS, et al. (2013) Computational investigation of roller-bearing premature-failure in horizontal-axis wind-turbine gearboxes. *Solids Struct* 2: 47–56.

24. Grujicic M, Chenna V, Galgalikar R, et al. (2014) Wind-turbine gear-box roller-bearing premature-failure caused by grain-boundary hydrogen embrittlement: A multi-physics computational investigation. *J Mater Eng Perform* 23: 3984–4001.

25. Grujicic M, Chenna V, Yavari R, et al. (2015) Multi-length scale computational analysis of roller-bearing premature failure in horizontal-axis wind-turbine gear-boxes. *Int J Struct Integ* 5: 40–72.